Exploring the nano-polishing mechanisms of Invar

Wan Wang[a], Dongpeng Hua[a], Dawei Luo[a], Qing Zhou[a,*], Stefan J. Eder[b,c], Shuo Li[a,*], Zhijun Wang[d], Haifeng Wang[a,*]

[a] Center of Advanced Lubrication and Seal Materials, Northwestern Polytechnical University, Xi'an, Shaanxi 710072, P.R. China

[b] AC2T research GmbH, Viktor-Kaplan-Straße 2/C, 2700 Wiener Neustadt, Austria

[c] Institute for Engineering Design and Product Development, TU Wien, Lehárgasse 6 – Objekt 7, 1060 Vienna, Austria

[d] State Key Laboratory of Solidification Processing, Northwestern Polytechnical University, Xi'an, China

Abstract

With the rapid development of nano-polishing technology, ultra-precise micro-nano components require tighter tolerances for the surface engineering of the Invar alloy. Due to its low hardness and high chemical activity, it is a challenge to obtain high-quality surfaces with a nanometric finish for Invar, and the mechanical mechanism guiding the nano-polishing process is also hard to derive experimentally. In this work, we studied the key influencing factors on the nano-polishing behavior of Invar by molecular dynamics simulation, and experiments were conducted to verify the simulation results. Our findings indicate that higher polishing speed and shallower polishing depth with optimized rolling torque can lead to a reduction of the subsurface damage as well as an improvement in polishing efficiency and surface quality. The nano-polishing mechanism is revealed, showing that effective removal occurs only in the plowing regime and the cutting regime, which require sufficient rolling/sliding depths. Furthermore, an analytic removal theory was developed that excellently describes and predicts the polishing behavior of Invar. Present work can provide a basis

E-mail address: zhouqing@nwpu.edu.cn (Qing Zhou)
shuoli2020@nwpu.edu.cn (Shuo Li)
haifengw81@nwpu.edu.cn (Haifeng Wang)

and technical support for the achievement of ultra-smooth and low-damage Invar surfaces, facilitating their wide applications in various significant fields.

***Keywords*:** Nano-polishing; Subsurface damage; Invar alloy; Molecular dynamics simulation

1. Introduction

Invar alloy, an $Fe_{65}Ni_{35}$ alloy with face centered cubic (FCC) structure and extremely low or no coefficient of thermal expansion in a wide temperature range [1-3], has attracted extensive research interest in recent years. In addition to an intriguing thermal expansion coefficient, its many extraordinary properties, such as excellent fatigue resistance and mechanical properties in low temperature environments, good ductility and toughness [4] together make Invar one of the most promising candidates for applications in aerospace engineering, precision instruments/tools, optical components and composite molds [5]. All these applications not only require outstanding mechanical performance, but also call for ultra-precise machining and high surface quality of the materials. Usually, a series of processing techniques such as cutting, grinding, lapping, or nano-polishing, are carried out to achieve an ultra-smooth surface of Invar [6, 7]. However, surfaces with high precision and few defects are difficult to obtain due to its low hardness and high chemical reactivity, making processing inefficient and costly. Therefore, understanding the material removal mechanism in a nano-polishing process is of vital importance for guiding low-damage machining and achieving high precision surfaces on Invar.

Aiming at improving the processing quality of materials, great efforts have been made to deepen the understanding of their processing behavior [8-12]. Among all these methods, high-speed polishing has thrived as a mainstream manufacturing technology to produce critical components with high surface quality [13]. However, the material removal and damage behavior during the nano-polishing process cannot be predicted

by traditional processing theories, and modern experimental techniques are inadequate to reveal the underlying deformation behavior, leaving the optimization of process parameters to achieve ultra-precision machining without effective guidance [14]. Molecular dynamics (MD) simulations have been proven to be a powerful tool to investigate the material removal mechanism at atomic scale. The effects of polishing speed [15-17], polishing depth [18-20], rotating velocity [21, 22], grain size [23, 24], normal pressure [25, 26] and work piece temperature [27] on the surface quality of the work piece can been systematically investigated based on MD simulations. Zhang et al. [28] studied the effects of grinding depths and speeds on the subsurface damage layer (SDL). The results showed that quantities of defects exist in the subsurface and the SDL is more sensitive to grinding depth than grinding speed. Li et al. [29] investigated the key influencing factors for subsurface damage and material removal, including tool speeds, tool radius, depth of cut, crystal orientation and grinding directions of copper. It was found that a higher grinding speed, a larger tool radius or a larger depth of cut would result in more chips and a greater temperature rise in the copper work piece, and a higher speed, a smaller tool radius, or a smaller depth of cut will reduce the damage thickness and improve the smoothness of surface. Meng et al. [30] found that the strain rate and thermal softening directly affect the formation of surface damage of silicon carbide. The results showed that the thermal softening effect at high strain rates determines the direction of the stress, and the thermal softening effect on the stress in the machined area exceeds the reduction in the growth rate of the dislocation generation. Yang et al. [21, 31] claimed that the self-rotation speed and sliding direction of the

abrasive particle significantly affect the morphology and quality of the sample surface in ultra-precision mechanical polishing of monocrystalline silicon and copper. Specifically, both the quantity and the volume of defects are the largest when the self-rotation velocity is equal to abrasive sliding velocity.

The above research showed that it was particularly important to investigate the influence of various parameters on the material removal mechanisms occurring during nano-polishing. However, most of the previous research focused on the material removal process and chip formation under various processing parameters while treating the abrasives as rigid bodies under pure sliding motion. However, in real polishing processes, the abrasives also feature some degree of rolling motion, which leads to different modes of workpiece deformation and removal mechanism in nano-polishing. Not many studies address these issues. In particular, until now nobody has undertaken a systematical study or set up a guiding theory of the polishing process for Invar despite its special material deformation mechanism and practical significance.

In this work, MD simulations were conducted to reveal the material removal behavior of Invar, and corresponding experiments with spindle rotation polishing were also conducted to verify the simulations. The effects of polishing mode (abrasive sliding or rolling), polishing speed and depth on the deformation characteristics and material removal of Invar were systematically investigated. With an emphasis on the motion mode of the abrasive particle, an insightful understanding of the plastic performance and removal mechanisms in the nano-polishing process is also provided. The result provides a guideline for improving the polishing precision, surface quality, and material

removal efficiency for Invar work pieces.

2. Methodology

2.1. MD model

In this study, the simulation process was conducted using the large-scale atomic/molecular massively parallel simulator (LAMMPS) [32]. The Open Visualization Tool (OVITO) [33] was utilized to show the structure. Dislocations were identified by the dislocation extraction analysis (DXA) [34, 35], and subsurface damage thickness (SDL) was visualized through common neighbor analysis (CNA) [36]. As a simplification, the model composed of a single abrasive particle (diamond with radius of 20 Å) and the $Fe_{65}Ni_{35}$ monocrystal Invar alloy with a FCC structure was constructed as shown in Fig. 1(a). The sample contains 452000 atoms of which Fe atoms account for 65% and the rest are randomly distributed Ni atoms, and has dimensions of ~24.86×10.66×10.66 nm^3 along *X*-[100], *Y*-[010] and *Z*-[001], respectively. The interactions between Fe and Ni atoms were represented by the second nearest-neighbor modified embedded-atom-method (2NN MEAM) potential [37]. The Lennard-Jones potential was adopted to describe interactions between C–Fe and C–Ni atoms with ε_{C-Fe} = 0.12 eV, σ_{C-Fe} = 2.71 Å, ε_{C-Ni} = 0.12 eV, and σ_{C-Ni} = 2.69 Å [38, 39], and the cutoff distance was set to 7 Å, while the abrasive particle is treated as a rigid body. The model was divided into three layers, namely the boundary layer, the thermostat layer and the Newtonian layer, as shown in Fig. 1(a). The boundary layer atoms (colored in red) were fixed to ensure the stability of the model. Through the velocity scaling method, the temperature of thermostat atoms (colored in blue) were maintained at 300 K to dissipate the heat generated during nano-polishing. The rest atoms in the Newtonian atoms (colored in yellow) followed the classical Newton's second law [22].

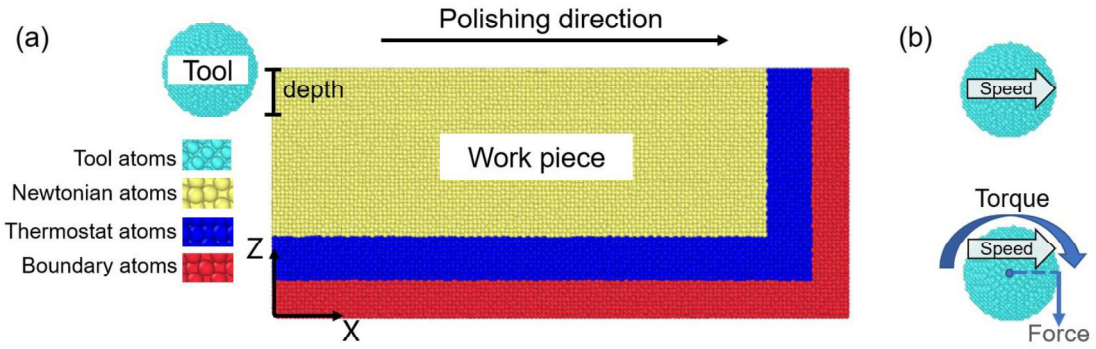

Fig. 1. (a) MD simulation model of the nano-polishing of Invar and (b) movement state of the abrasive (sliding vs. rolling).

At the beginning, the abrasive particle was placed 10 Å away from the left end of the work piece. Periodic boundary conditions were applied in *X* and *Y* directions, while the bottom surface was fixed, and the top surface free. The simulation process consists of two stages: relaxation and nano-polishing. During the relaxation process, the entire model was relaxed at 300 K for 500 ps under the NPT ensemble to achieve equilibrium configuration. In the nano-polishing process, an NVE ensemble was applied to the entire model, while only the temperature of the thermostat atoms was controlled. The movement of the abrasive can be divided into two components (i.e., sliding and rolling), as shown in Fig. 1(b). The sliding speed for the abrasive was 50, 100, 150 and 200 m s^{-1}, and the polishing depth *h* was set to be 5, 10, 15, and 20 Å to assess the various nano-polishing mechanisms. In this study, relatively small values of polishing depth were chosen compared to previous reports to focus on nanoscale and sub-nanoscale polishing [40]. Besides, a rolling torque *T* of 0.5-2 eV (corresponding to a force of 4-16 × 10^{-5} μN applied to the abrasive as shown in Fig. 1(b)) was also assigned to the particle to consider the effect of rolling on the polishing behavior [41]. These input variables affect the abrasive-work piece interaction, including material removal, subsurface damage, and the temperature distribution. The final polishing results are determined by the synergetic action of the above process parameters.

2.2. Experiments

A rotary-type polishing machine (YM350A-03, Nanjing, China) was used in the Invar polishing experiments, and the schematic diagram of the polishing process is shown in Fig. 2. Cylindrical Invar samples with a diameter of 20 mm were used in this study, and their original surface roughness R_a was approximately 50 nm. The polishing experiment was conducted at room temperature. The slurry with abrasive particles was prepared, and the polishing pressure and time were 30 N and 10 min, respectively. The spindle speed was scaled down in proportion (V: 1000, 1500, 2000 and 2500 r/h) to the simulated speed to study the sliding speed effect on the surface roughness R_a and material removal rate (MRR).

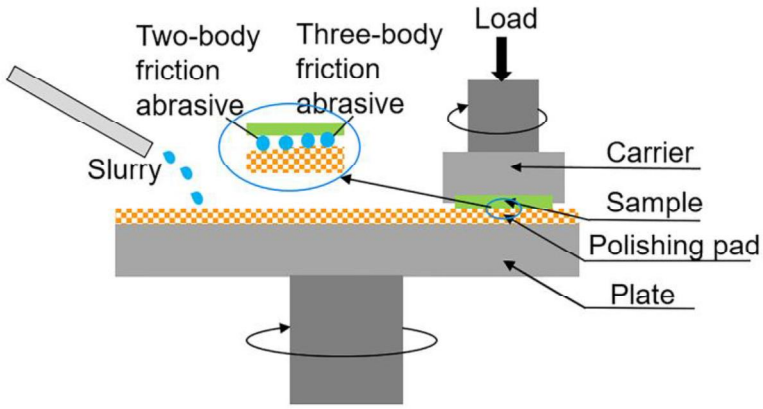

Fig. 2. Schematic diagrams of nano-polishing setup.

The surface topography and roughness were measured using a 3D optical surface profiler with a scanning area of 100 μm × 200 μm (NPFLEX, Bruker, USA). The MRR was obtained from the volume loss of material before and after polishing. Both results were the averaged value of 5 areas that were evenly distributed over the sample surface, and error bars were based on standard deviation.

3. Results

3.1 MD simulations in nano-polishing

3.1.1. Effect of polishing speed

Sliding speed is the main parameter that affects the machined surface integrity during processing, and its effect on the nano-polishing response is shown in Fig. 3. In Fig. 3(a), as the sliding speed increases, the transverse force and normal forces gradually increase, except for a slight drop of normal force at 200 m s^{-1}. The temperature change of the Newtonian layer at various sliding speeds with the sliding distance d_s is shown in Fig. 3(b). It can be seen that the temperature rises with the polishing distance, originating from extra kinetic energy produced by polishing [16]. The friction and strain energy released by the deformed region will be converted into polishing heat, resulting in higher thermal energy when polished at a higher speed. Fig. 3(c) shows cross-section snapshots of the Invar under various polishing speeds. The highest temperature is produced in the chip and the abrasive trail region, originating from the friction energy at the abrasive-work piece interface and the plastic deformation occurring in the primary shear zone [42]. As a result, the internal crystal structure of the work piece will be destroyed, forming an SDL. The chip formation is caused by shearing and stress-driven dislocation motion in front of the abrasive [43]. In addition, shallower grooves are formed with the increase in the polishing speed. This is because the higher temperature at the processed surface leads to the thickening of the SDL, which has a higher hardness than the defect-free work piece and is more wear-resistant due to its amorphous characteristic [44, 45].

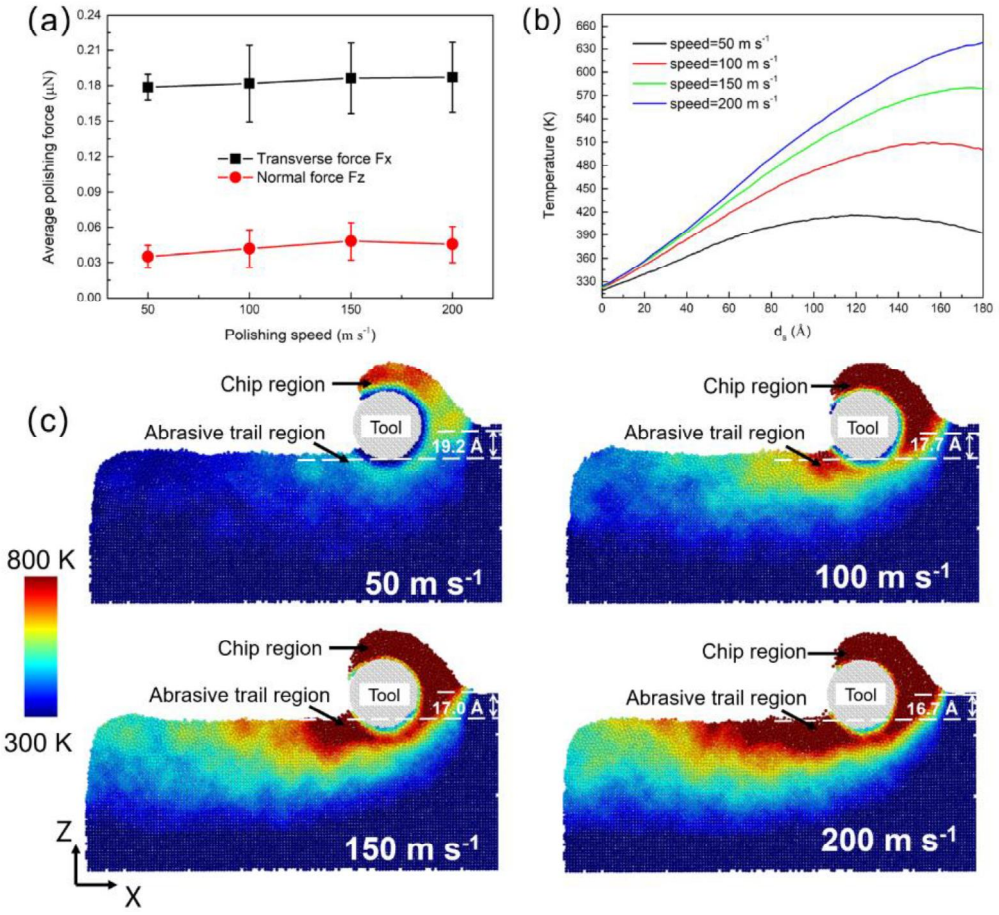

Fig. 3. (a) The average polishing forces as a function of the polishing speed, (b) variation of the average temperature over polishing distance, and (c) the distribution of the temperature at a polishing distance of 180 Å for four different polishing speeds (h = 20 Å).

The polishing quality can be evaluated in terms of the stacking height, surface roughness, SDL and amorphous atoms formation [29]. Fig. 4(a) displays the stacking height at different polishing speeds. During the polishing process, the atomic stacking height increases with the polishing distance, and the chip heights at the polishing distance of 180 Å is shown in the inset of Fig. 4(a). As the polishing speed increases, the maximum height of the chip first increases, and then begins to decrease at a polishing speed of 150 m s^{-1}. Fig. 4(b) shows the surface roughness and MRR at different polishing speeds. The surface roughness R_a is obtained as $\delta = \sum_{i=1}^{N} \left| h_i - \bar{h} \right|$, where N represents the number of atoms on the grooved surface, h_i is the surface atom

height along the polishing direction, and $\bar{h}$ is the average topographic height of the grooved surface. As indicated in Fig. 4(b), the groove roughness first decreases and then increases with rising polishing speed. The removed materials are defined as the chip atoms above the original surface [46], and the MRR is the volume of removed material atoms per unit time. As the polishing speed increases, the maximum height of the chip accumulated in front of the abrasive and the MRR increase accordingly due to the higher plasticity of the work piece at higher temperatures [19]. However, when the polishing speed is higher than 150 m s^{-1}, the chip height decreases since more atoms in front of the abrasive flow back into the groove from the lateral sides. This leads to a decrease in MRR at higher polishing speed, indicating that blindly increasing the polishing speed cannot achieve a higher MRR [47], which is inconsistent with the report of Li et al. [17] where the stacking height was reduced, but the MRR consistently improved with increasing polishing speed.

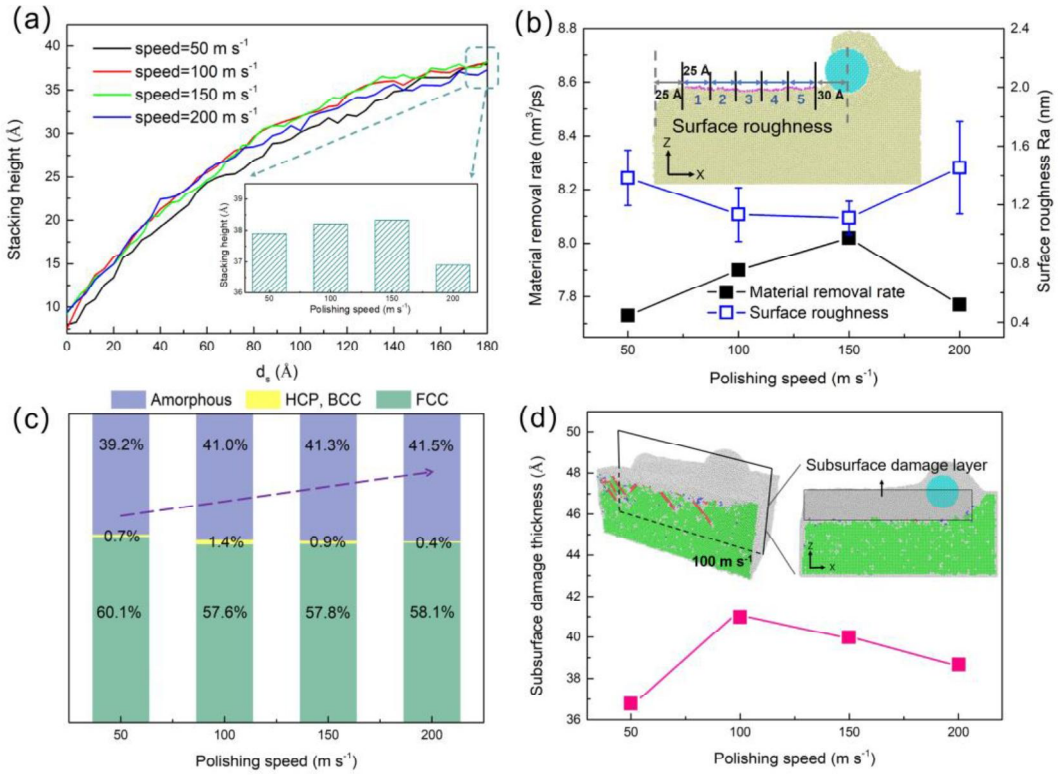

Fig. 4. The variations of (a) the stacking height, (b) the MRR and surface roughness, (c) the

percentage of work piece structure after nano-polishing, (d) the SDL thickness with the polishing speed. Atoms are colored according to CNA (FCC structure in green, amorphous atoms in gray, BCC structure in blue, and HCP structure in red) at a polishing distance of 180 Å and a polishing depth of 20 Å. The error bars for R_a are calculated from five different regions of the grooved surface in the marked purple area, as shown in the inset of Fig. 4(b).

Many studies [15, 30, 48] have focused on the observation of amorphous and other lattice changed atoms, while lacking the study of the original lattice changes. This paper starts from the original lattice (FCC) occupation ratio to better reflect the internal damage of the work piece. The crystal structure occupancy of the work piece atoms and the dependence of the SDL thickness after polishing on the abrasive speed is shown in Figs. 4(c) and (d). It can be seen that the work piece atoms after polishing are mainly of FCC and amorphous structure in Fig. 4(c). During polishing, the work piece under the abrasive is scratched, and the crystalline structure in the groove region is destroyed and transformed into an amorphous structure due to severe plastic deformation as shown in the inset of Fig. 4(d). However, the amorphous structure formation in other regions is caused by thermal activation as the part of work done by the cutting and extrusion process of the abrasive is converted into internal energy [49]. Besides, after polishing, some atoms suffering elastic deformation can recover to their original structure, which indicates that the amorphous phase transition of Invar is partially reversible [17, 28].

As shown in Fig. 4(c), the percentage of atoms in the amorphous state rises slightly, and the ratio of atoms in the FCC structure decreases slightly as the speed increases. This can be attributed to the heat-affected region of the work piece grows with the increase of polishing rate (see Fig. 3(c)). The SDL thickness is the distance from the surface of the workpiece to the lowest point of the continuous amorphous structure [50]. As shown in Fig. 4(d), the thickness of the SDL first increases with rising polishing

speed, but as soon as the grinding speed is higher than 100 m s^{-1}, the thickness of the SDL begins to decrease. The formation of an SDL mainly comes from the disruption of the FCC lattice in the subsurface layer, and in addition to the conversion of damaged FCC structures into amorphous states, there is a small portion of HCP and BCC structures indicating the dislocation behavior [51]. Meanwhile, the temperature increase at speeds of 50-100 m s^{-1} promotes the formation of defects, but the speed of 150-200 m s^{-1} is too fast for defects to form in time, resulting in a reduced subsurface damage layer at the highest considered speed [23]. These results confirm that the abrasive can have an optimum polishing speed that combines the best removal efficiency with the best surface quality.

3.1.2. Effect of rolling torque

In addition to the effect of sliding speed, in real polishing processes, the rolling motion of the abrasives significantly affects the polishing quality [52, 53]. In order to provide a more comprehensive understanding of the polishing behavior, in this section, MD simulations are conducted to elucidate the effect of rolling torque on the surface quality, surface/subsurface damage, and MRR when polishing Invar.

The rolling motion of the abrasive is set up with a torque applied on the basis of sliding motion as shown in Fig. 1(b). During the rolling movement, both the average transverse force and normal force decrease as the rolling torque increases, as shown in Fig. 5(a). The average temperature of the work piece increases with the torque and the polishing distance, as shown in Fig. 5(b). During the progress of the polishing process, severe stresses accumulate, leading to the collapse of structure and the release of strain energy, accompanying a rapid rise in work piece temperature, a similar outcome to Nguyen *et al.* [54]. Then, the temperature reaches a state of dynamic equilibrium as shown in Fig. 5(b). On the other hand, the temperature rise in the work piece is

dependent on the rolling torque. In Fig. 5(c), it can be seen that high temperature zones exist on both the leading and the trailing ends of the abrasive, and that they are considerably larger than that for the pure sliding motion in Fig. 3(c), which might originate from a stirring effect of the abrasive [54].

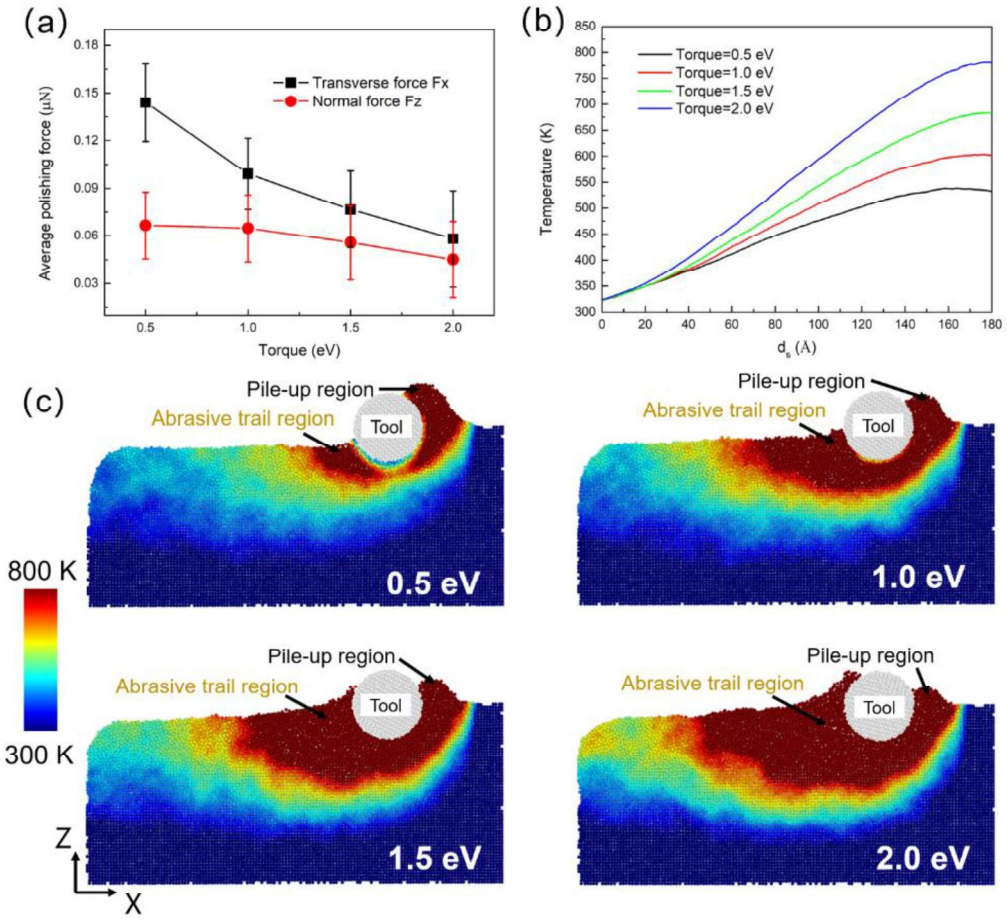

Fig. 5. (a) The curves of the average polishing force, (b) variation of the average temperature, and (c) the distribution of the temperature at a polishing distance of 180 Å under different rolling torques (V = 100 m s^{-1}, h = 20 Å).

Fig. 6(a) shows the variation curve of the stacking height with the polishing distance under various rolling torques. The stacking height shows a decreasing trend with the increasing rolling torque. This is because in the polishing process, the work piece atoms adhering to the surface of the abrasive are forced back to the surface of the work piece again as they continue to roll with the abrasive. Fig. 6(b) shows the relationship of rolling torque to MRR and surface roughness. It can be seen that the

MRR is negatively related to the rolling torque, and the optimum surface quality (with the lowest surface roughness) is obtained when the rolling torque is 1 eV, as shown in Fig. 6(b). Compared with the pure sliding motion in Fig. 4(b), a greater MRR is produced at a rolling torque of 0.5 eV. The crystal structure occupancy of the work piece atoms and the thickness of the SDL with different rolling torques are compared in Figs. 6(c) and (d). When the torque is added to the abrasive particle, the number of amorphous atoms and the thickness of SDL first show a decreasing trend followed by an increase, and the percentage of FCC structure atoms is almost the same as for pure sliding motion. The addition of torque can reflect the rolling friction in addition to sliding of the abrasive during the nano-polishing process. However, the effect of rolling friction is limited at a torque of 0.5 eV, and friction is still dominated by sliding. The sharp increase in the temperature inside the work piece expands the workpiece volume, resulting in a higher MRR and more severe SDL [21]. With the increase of the torque to 1 eV, the contribution of rolling exceeds the contribution of sliding in friction, leading to a reduction of interaction between the work piece and the abrasive. Hence, the polishing force and the SDL are significantly reduced. Further increasing the torque of the abrasive, the atomic movement intensifies due to the sharp increase in the local temperature of the work piece (Fig. 5(c)), destroying the original FCC structure and prompting more defects and amorphous regions in the SDL. Also, the surface is strongly stirred due to the adhesion phenomenon between the abrasive and the work piece atoms, generating some protrusions (raised parts on both sides of the groove) and asperities (roughness features within the groove). As a result, the groove is not as smooth as for sliding motion dominated polishing [54]. Based on the above, the best polishing quality of the work piece is obtained when the torque of the abrasive particle is approximately 1 eV.

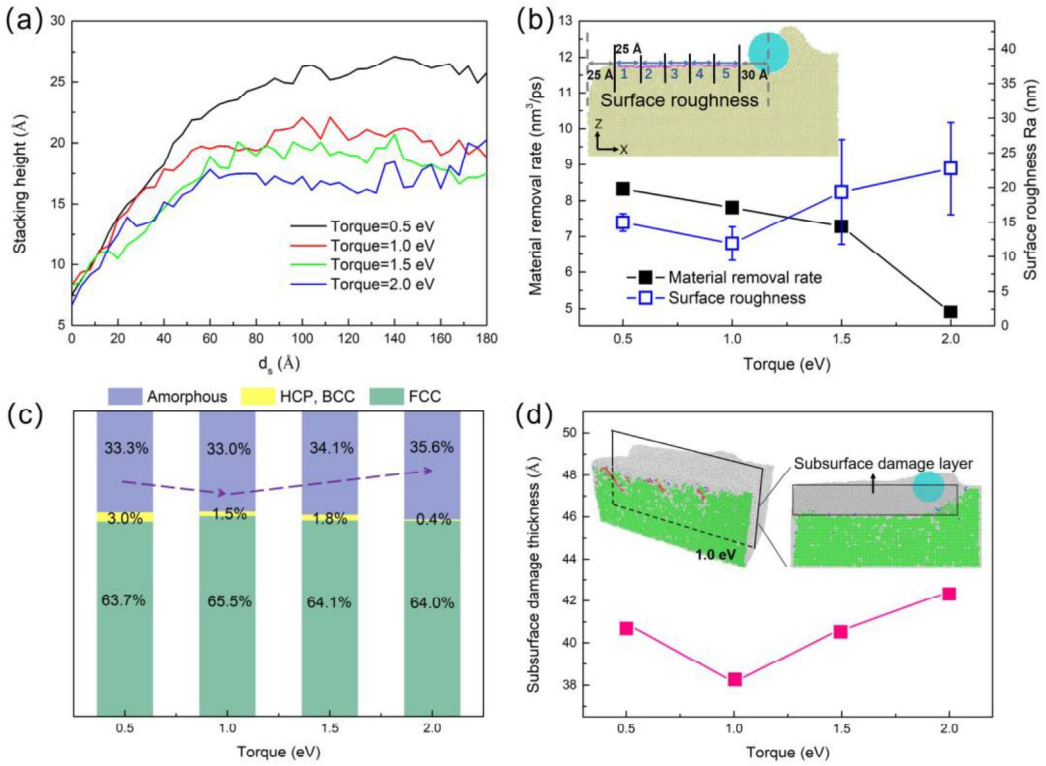

Fig. 6. Various data diagrams at different rolling torques after a polishing distance of 180 Å (a) the variation curve of stacking height with the polishing distance, (b) the MRR and surface roughness, (c) the percentage of work piece structure after nano-polishing, and (d) variations of SDL thickness to the rolling torque. Atoms are colored according to CNA values (the FCC structure in green, the amorphous atoms in gray, the BCC structure in blue, and the HCP structure in red) at a polishing speed of 100 m s^{-1} and a polishing depth of 20 Å.

3.1.3. Effect of polishing depth

Finally, the removal depth of the abrasive is another important parameter that determines the surface quality, subsurface damage and MRR of Invar. At different polishing depths, the removal of work piece material can be classified into various regimes: non-wear regime, condensing regime, adhering regime, plowing regime and cutting regime [55]. In the non-wear regime, only elastic deformation is produced; the condensing regime corresponds to polishing at a slightly greater depth, but still without material removal; the adhering regime refers to atoms that are stuck to the abrasive and then removed; the plowing regime means that atomic clusters or pile-up are formed due

to plastic deformation; cutting regime features severe material removal in the form of chip formation. Fig. 7 shows the surface morphologies of the work piece at various polishing depths after a polishing distance of 180 Å at 100 m s^{-1}. As shown in Figs. 7(a1)-(a4), the surface morphology and wear regime changed significantly for different sliding depths. Different from the observation of Nguyen et al. [48], the non-wear regime does not appear in the sliding process of Invar although a same depth of 5 Å is adopted. The abrasive in this case generates a pile-up and a discontinuous groove, and the groove shows obvious evidence of elastic recovery. The formation of local grooves (blue regions) indicates a transition state between the plowing removal and the adhering regime. At a depth of 10 Å, the chip in front of the abrasive gradually increases and the work piece is strongly wiped out, showing a transition state between the plowing removal and the cutting regime. At depths of 15 Å and 20 Å, it can be readily observed that a large number of the surface chips are formed in front of the abrasive and on the lateral sides of the groove, indicating a cutting regime.

In summary, as the polishing depth increases, the length and width of the groove, the chips accumulated in front of the abrasive, and the lateral flow gradually increase. Eventually a horseshoe-shaped accumulation forms in front of the abrasive particles. In order to reveal the underlying reason for the formation of the surface stacking topography, we discuss it by the available slip directions of Invar in Fig. 7(c). During polishing along the [1 0 0] direction, all slip direction <1 1 0> for Invar was exactly symmetrical, as shown in Fig. 7(c). The schematic shows how different <1 1 0> slips act for the considered polishing systems to generate the surface pile-ups, and the slip vectors pointing downwards or backwards are omitted. For the [1 0 0] scratch direction, there are two slip directions that point upwards towards the surface and lead to lateral pile-up. One slip direction points directly into the forward direction, which leads to

frontal pile-up. They are perpendicular to the scratch directions and produce a horseshoe-like lateral pile-up pattern [39]. However, as the sliding depth increases, the stacking topography of the work piece appears slightly asymmetric due to the uneven plastic deformation of the work piece surface. Also, the corresponding dislocation distribution map of Fig. 7(a4) is shown schematically in Fig. 7(c). The atomistic and irregular nature of the dislocation nucleation and slipping processes can result in an uneven plastic zone around the abrasive and an slightly asymmetric surface [56, 57], which may affect the surface integrity of the work piece during the nano-polishing process. As shown in Fig. 7(c), the dislocations accumulate mainly in the [011] directions, resulting in a shift of the removed atoms in the direction of dislocation accumulation. Therefore, the removed atoms mainly accumulate at the right of the groove, which is confirmed in Fig. 7(a4).

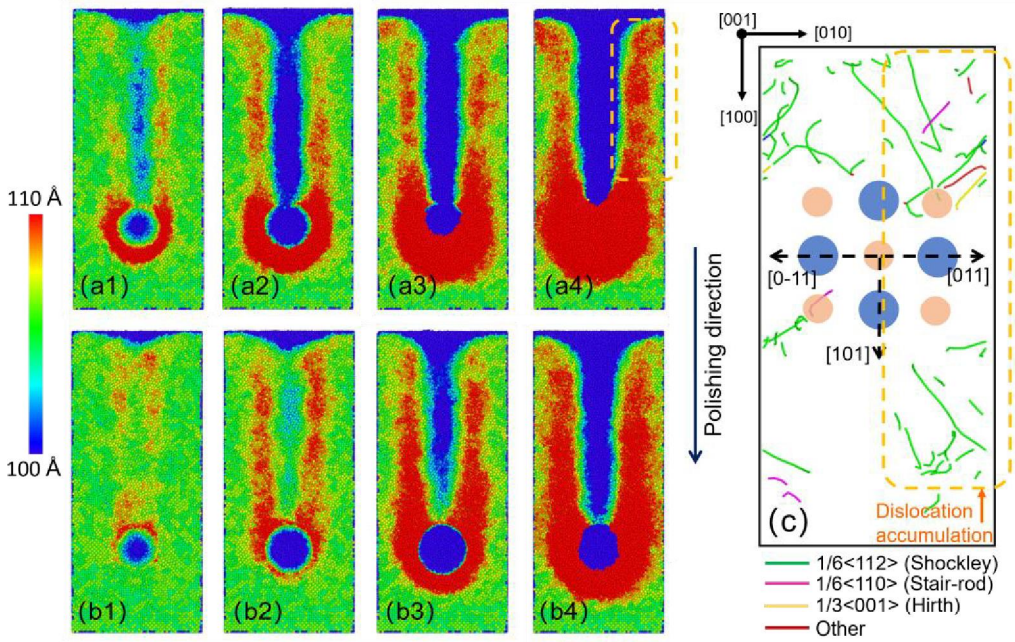

Fig. 7. Surface morphology at polishing depths of (a1)-(a4) 5, 10, 15 and 20 Å in sliding motion, and (b1)-(b4) 5, 10, 15 and 20 Å in the rolling motion (V = 100 m s^{-1}, T = 1 eV), where atoms are colored according to their Z coordinate. (c) Synopsis of slip directions and dislocation distribution at the sliding depth of 20 Å in the polished work piece, where schematic large blue (small orange)

circles indicate the first (second) layer atoms, and black (red) lines indicate the atom (dislocation) stacking direction.

For the rolling motion, however, an Invar specimen will experience different wear regimes in comparison with sliding motion. Figs. 7(b1)-(b4) show the surface morphologies of the work piece at different rolling depths when the polishing speed is 100 m s^{-1} with the rolling torque of 1 eV. At 5 Å and 10 Å, the condensing and adhering regimes, respectively, dominate as there are only few atoms removed. At depths of 15 Å and 20 Å, the plowing regime appears as more atoms wiped out. Compared to the sliding movement, as demonstrated in Fig. 7, the rolling motion requires a deeper depth to enter the plowing regime.

In order to show the material removal effect more intuitively, the MRR and surface roughness at different sliding and rolling depths were summarized in Fig. 8(a). It can be seen that the MRR increases as the depths increase both in sliding and rolling motion. Generally, the sliding movement removed the work piece atoms more efficiently than the rolling movement. The sliding removal mechanism is similar to the cutting or plowing with the formation of a big cluster of pile-up or chips. In the rolling movement, the atoms are gradually transferred by the adhesion of the abrasive surface when it rolls over the work piece surface. Therefore, the removal capacity is limited by the contact area of the abrasive and the surface adhesion can be saturated [48, 52]. The surface roughness was shown in Fig. 8(a). As the polishing depth deepens, the surface roughness during sliding tends to increase first and then decrease, while the surface roughness during rolling keeps increasing. The roughness is relatively low at a polishing depth of 5 Å, where only one or two atomic layers are removed and no

obvious grooves and ridges are formed [47]. Different from refs [22, 58, 59], our work shows that the roughness of sliding is not always better than rolling. At polishing depths of 15 and 20 Å, more atoms of the work piece are removed by the adhesion effect of the abrasive in rolling motion, leading to an uneven and worse surface quality than for sliding motion. These results suggest that the surface quality can only be improved by adding an appropriate rolling torque.

Fig. 8(b) shows the number of atoms in contact with the abrasive at different polishing depths, and the contact atoms are defined as atoms with a distance less than $2^{1/6} \times \sigma_{C\text{-}Ni}$ from the abrasive [60]. It can be seen that the contact area is proportional to the polishing depth, while the difference in the number of atoms in contact with the abrasive in the sliding and rolling motion is not significant. Figs. 8(c) and (d) display the change in structure of the work piece and the thickness of the SDL. The results suggest that the percentage of amorphous atoms in the work piece and the thickness of the SDL are positively correlated with the polishing depths, while FCC structure atoms show the opposite trend. Besides, at polishing depths of 5 to 15 Å, the rolling motion gives rise to serious SDL formation, but the difference between sliding and rolling is minor for both amorphous and FCC structures. However, at a polishing depth of 20 Å, the contact area between the abrasive and the work piece increases as shown in Fig. 8(b), and the area affected by the high temperature inside the work piece is much larger. The high friction force and temperature (0.18 μN, 495K in sliding motion and 0.10 μN, 575K in rolling motion) at the work piece surface promote the avalanche of internal defects, leading to a collapse of crystal structure and an increase in the amorphous state

[49]. Furthermore, compared with the adjusting polishing speed and the rolling torque, reducing the polishing depth (or normal pressure) could be more effective in regulating the subsurface quality of the work piece.

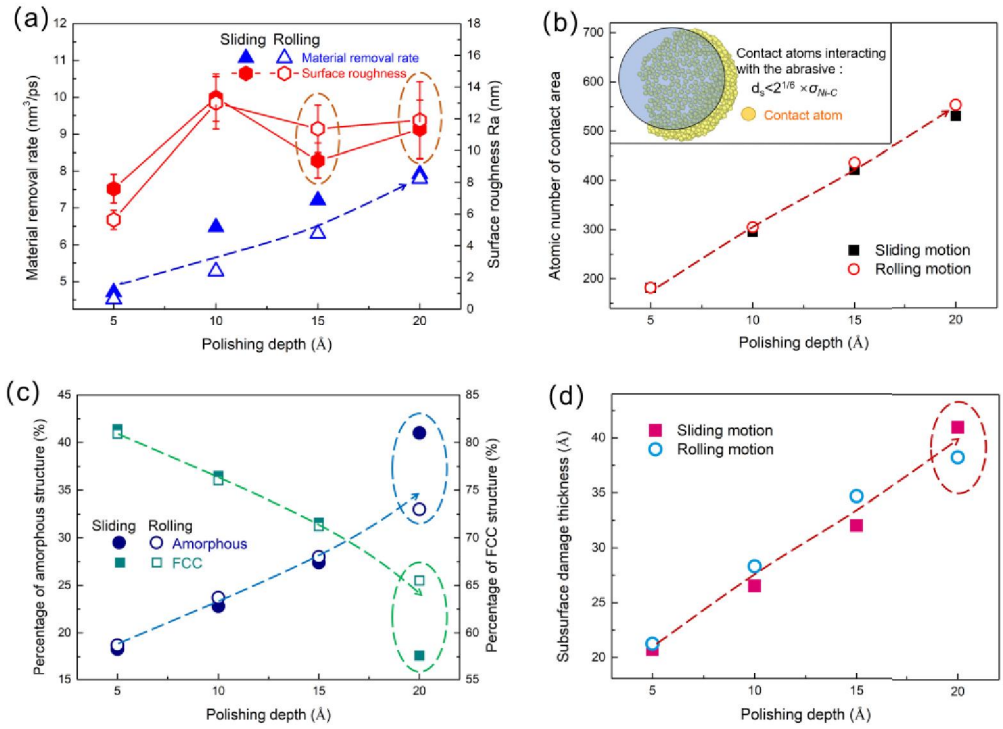

Fig. 8. The relationship of (a) MRR and surface roughness, (b) the amorphous/FCC atoms percentage, (c) the SDL thickness, and (d) the atomic number of contact area with the polishing distance of 180 Å at different sliding and rolling depths (V = 100 m s^{-1}, T = 1 eV).

3.2. Experimental validation

Morphologies of surfaces, surface roughness Ra and MRR polished with different spindle rotation speeds are shown in Fig. 9. From the surface morphology images, it can be seen that the topographies of different spindle speeds exhibit similar patterns, and there are prominent wave crests and valleys on the polished surface. At low speeds, the grooves on the polished surface are wider and leave a certain amount of protrusion. At high speeds, the grooves formed are shallower, which is consistent with the simulation observations in Fig. 3(c) and Zhu et al. [61] reported. However, a detailed

examination revealed that the surface roughness tends to decrease first and then increase as the spindle speed increases as shown in Fig. 9(e), while the MRR shows an opposite tend in Fig. 9(f). Therefore, it can be concluded that a moderate speed is desired for achieving the highest MRR and smoothest surface when polishing Invar. The results of MRR and surface roughness observed in experiments (see Figs. 9(e) and (f)) are consistent with the results measured in the nano-polishing simulations. While some researchers have debated the usefulness of MD simulations because the simulated polishing speeds are much higher than the experimental polishing speeds [62], making it impossible to quantitatively compare the MD simulation results with the experimental results, the scalable trend of the intrinsic performance can be qualitatively compared with experimental parameters to reproduce the underlying physics behind the results [19, 20]. These results demonstrate that MD simulations have practical significance for studying the behavior of atomic material removal during nano-polishing. During the speed-dependent abrasive polishing process, the abrasives' movement at different polishing depths are also accompanied by rolling motions [41]. Therefore, as the experimental technique lacks any details about the variation of force, temperature and subsurface structure, the analysis of MD simulation results under different polishing speeds, torques and depths certainly has guiding significance for actual polishing.

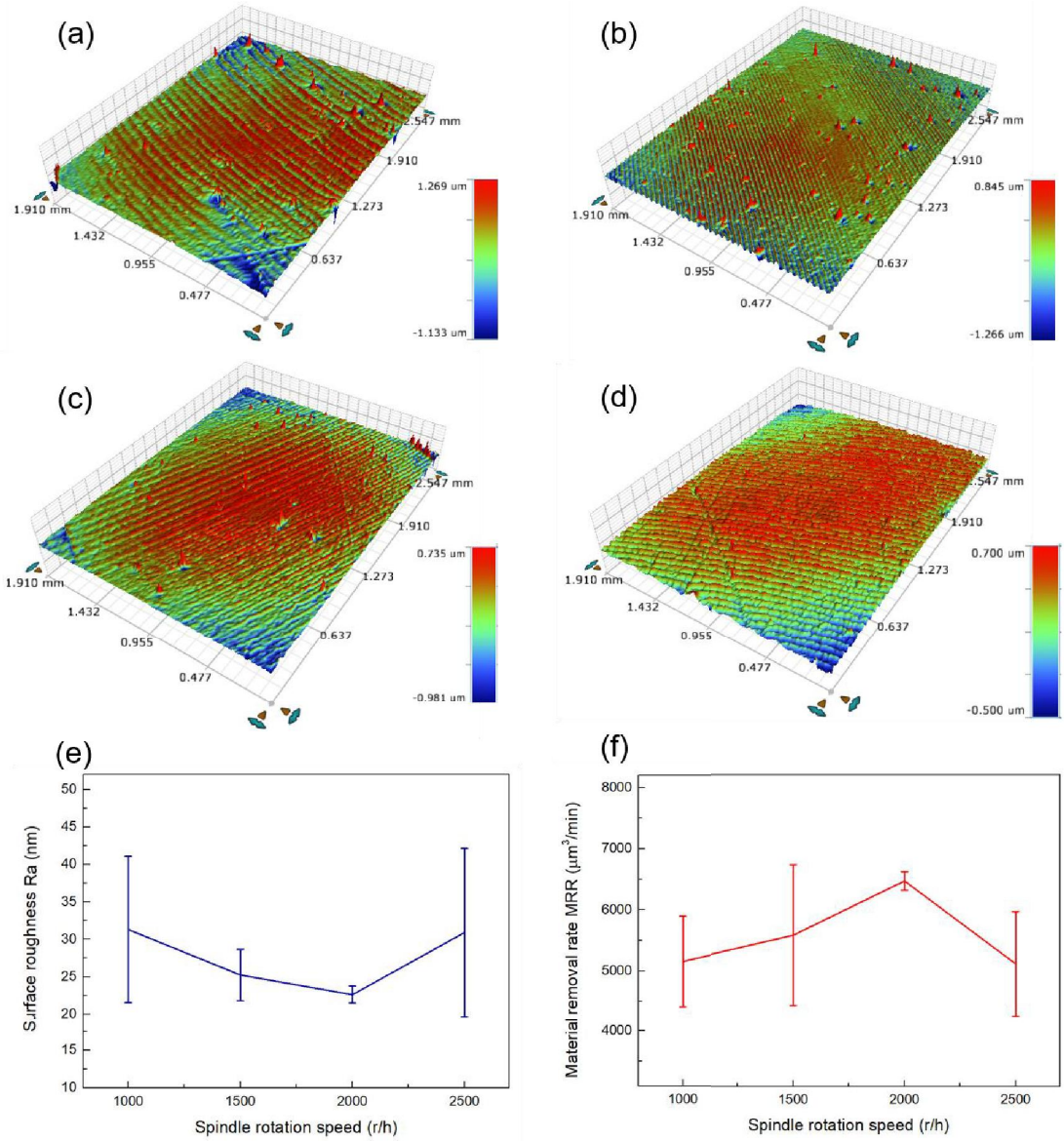

Fig. 9. (a)-(d) Surface morphology of polished Invar using four different spindle rotation speeds, (e) surface roughness Ra, and (f) MRR.

4. Discussion

4.1. Nano-polishing mechanism

In order to study the atomistic material removal mechanism, the atomic trajectory of the topmost layers is tracked during the nano-polishing process, as shown in Fig. 10. Each surface layer was labeled with a different color, and the rest was set to the same modest gray. The snapshots in Fig. 10 show the atomic distribution at various polishing

(sliding and rolling) depths. Fig. 10(a1) indicates that two atomic layers are removed after sliding at a depth of 5 Å. When the polishing depth exceeds 5 Å, critical layers that are partially removed can be identified, e.g., light yellow for 10 Å, green for 15 Å and light blue for 20 Å, as shown in Figs. 10(a2)-(a4). Above this critical layer, all the atoms move upwards along the diamond tool edge to form a chip, while the atoms below are pressed downward to form a machined surface. Approximately four, six and nine layers of atoms were removed at polishing depths of 10, 15 and 20 Å respectively. For all the cases, it was found that the distance from the critical layer to the tool bottom was approximately 5–6 Å, indicating the minimum cutting thickness for the work piece, which is also the critical depth for transformation between cutting and plowing [48]. In addition, the groove depths after polishing are 3.5 Å, 7 Å, 12.5 Å and 17.7 Å for polishing depths of 5 Å, 10 Å,15 Å and 20 Å, respectively. Obviously, the groove depths are shallower than the polishing depth due to the elastic recovery of the work piece material.

On the other hand, the atomic distributions within the work piece at different rolling depths are shown in Figs. 10(b1)-(b2). In Fig. 10(b2), only a few atoms are removed at a rolling depth of 5 Å, and the monoatomic layer removal only occurs at a polishing depth of 10 Å. With the rolling depth exceeding 10 Å in Figs. 10(b3) and (b4), pile-up occurs in front of the abrasive for the first time. Also, critical layers in yellow and dark green are identified at rolling depths of 15 and 20 Å, respectively. At rolling depths of 20 Å, the distance from the critical layer to the tool bottom is 10-11 Å, which is much larger than that in sliding motion. Besides, the pile-up height and groove depth

of rolling motions are shallower than the sliding case, exhibiting higher elastic deformation and lower material removal for the rolling motion.

The wear mechanism at different depths as illustrated in Figs. 10(a5) and (b5). Point A indicates the transition point between the cutting and plowing regime in sliding motion, and the transition point between the plowing and adhering regime in the rolling motion [63]. Only when the polishing depth h is greater than the minimum cutting thickness h_{min}, pile-up or a chip can be formed [64], and the critical atomic layer at point A is either moved upward or pressed downward along the abrasive particles. To summarize, the chip is formed in the cutting regime in sliding motion and the pile-up is formed in the plowing regime in the rolling motion.

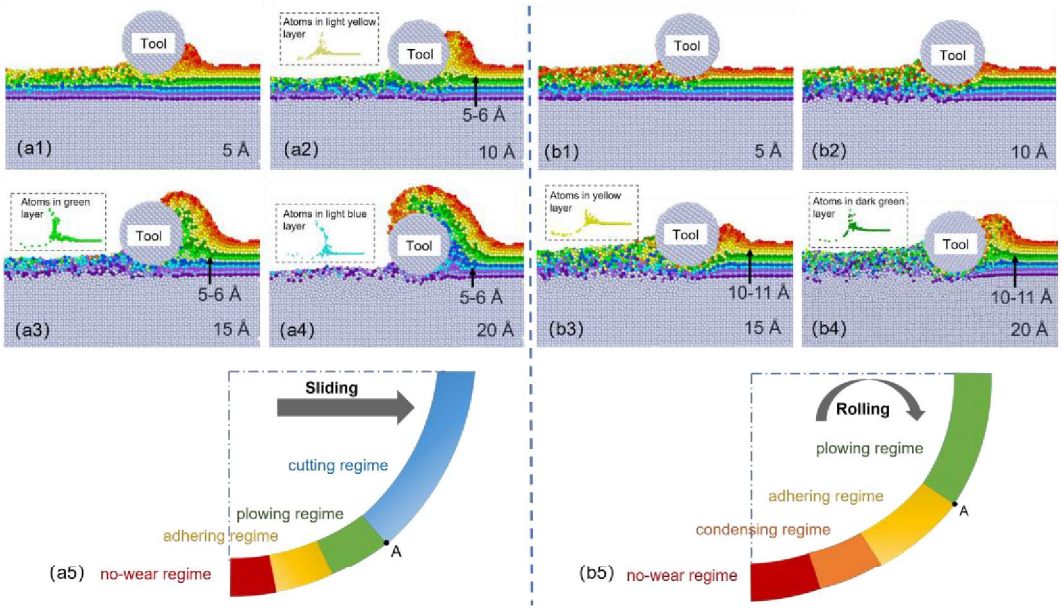

Fig. 10. Atomic distribution of Invar at different sliding depths with the polishing distance of 180 Å and schematic diagram for wear mechanism: (a1)-(a5) sliding motion, and (b1)-(b5) rolling motion (V = 100 m s^{-1}, T = 1 eV)

To obtain insight into the deformation mechanism during nano-polishing and to understand the influence of polishing depth on the defect behavior, Fig. 11 shows the

instantaneous distribution of dislocations in the SDL for a range of sliding and rolling depths. It can be clearly seen that the SDL is mainly composed of Shockley dislocations and Stair-rod dislocations that are located beneath the amorphous layer. Hirth and other dislocations are found only at a sliding depth of 20 Å as shown in Fig. 11(b4). The dislocations initiate and propagate during nano-polishing, leaving behind an ever-increasing SDL. Fig. 11 also shows the thickness of the SDL (gray area) at the later stage of polishing at different polishing depths. It can be clearly seen from the figure that there is a significant difference in the thickness of SDL between the sliding and rolling motion. At a polishing depth of 5 to 15 Å, the thickness of the SDL produced by sliding motion is shallower, but at a polishing depth of 20 Å, the trend is the reversed. This is because the rolling motion severely impacts the work piece in addition to plowing when the polishing depth is low. Since the rolling mechanism tends to push the work piece atoms downward, causing the location of its high-stress zones to be located mainly directly below the abrasive, the high-stress zones of the work piece in the rolling motion reach higher values than the high-stress zones for pure sliding motion. Thus, this complex stress state accelerates the collapse of the surface structure and the formation of an amorphous region.

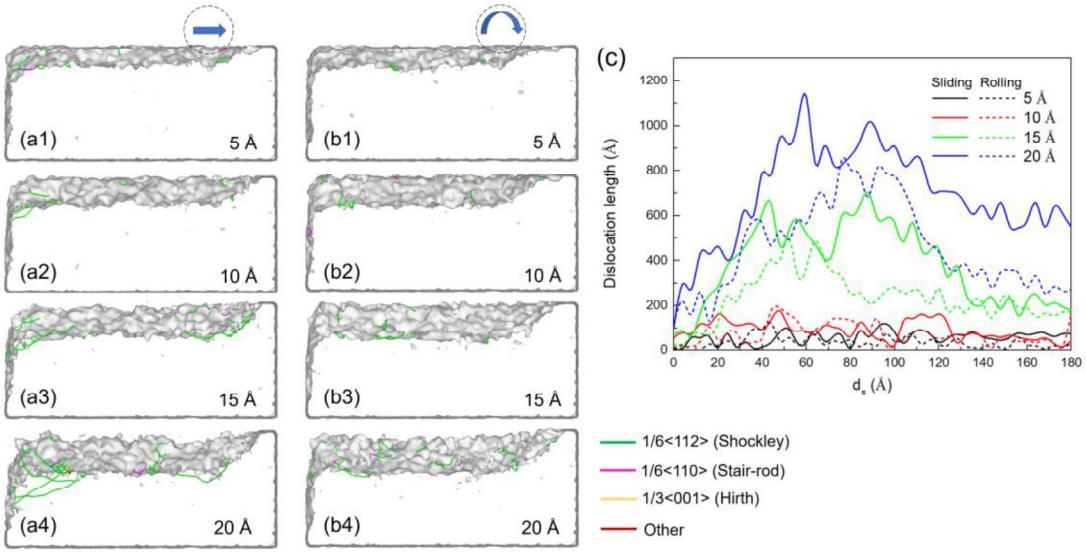

Fig. 11. The distribution of dislocations in Invar at a sliding velocity of 100 m s^{-1} for various polishing depths under sliding and rolling motion: (a1-a4) depths of 5, 10, 15 and 20 Å, (b1-b4) depths of 5, 10, 15 and 20 Å with a rolling torque of 1 eV. (c) Variation curve of dislocation line length with the distance under different polishing depths

However, when the abrasive penetrates the work piece deeper, the particle impact effect on surface is significantly reduced. In this case, the rolling will weaken the plowing effect, as it will push front atoms downward, leading to a reduced material removal (Fig. 10(b4)). For pure sliding motion without rolling, more irreversible damage is extended into the interior of the work piece, resulting in some unrecoverable dislocations and larger SDL. Also, the variety and number of dislocations are much greater than for the rolling motion as shown in Figs. 11(a4) and (b4). A statistical analysis of dislocation features under various polishing depths is shown in Fig. 11(c). Fig. 11(c) plots the change of the dislocation length over the polishing distance for various polishing depths. It can be seen that the dislocation length is positively correlated with the polishing depth, which can be ascribed to two aspects. On one hand, the deformed region increases with the polishing depth, and on the other hand, the

internal temperature and energy of the work piece gradually increase, leading to more intensified nucleation and expansion of dislocations, so the dislocation density increases. Moreover, at smaller polishing depths (5 Å and 10 Å), the removal regime of the abrasive is similar and the removal rate of the work piece is lower, so fewer dislocations are generated in sliding and rolling motion, leading to a high-quality surface. When the polishing depth increases to 15 and 20 Å, the dislocation line length shows a tendency to increase first, then decrease, and finally stabilize. This is because the plowing regime is the main removal mechanism under this condition, and the rise in temperature promotes the nucleation of dislocations, resulting in an increased dislocation density. In the later stage of polishing, the annihilation of dislocations in the center of the groove and the accumulation of dislocations at the abrasive front. More dislocations are annihilated in the grooves than are newly created in front of the abrasive, resulting in a decrease of the total dislocation density, which is in accordance with the results of Gao et al. [39]. Besides, at polishing depths of 5, 10, and 15 Å, the dislocation length gradually saturates to a similar value as the polishing distance approaches 180 Å. At a polishing depth of 20 Å, sliding motion leads to a higher dislocation density than rolling motion.

4.2. Analytical model

Generally, the transverse force would provide shear stress to enable dislocation movement within the deformation zone, while the normal force produces the compressive stress on the processed surface [65]. Fig. 12 presents the average polishing forces at various depths of 5-20 Å and at a polishing rate of 100 m s^{-1}. In general, the friction force mainly depends on the plowing force and the adhesion force. The deeper

the polishing, the greater the plowing force. The adhesion force is related to the vertical projected area of the contact between the abrasive and the work piece [66]. Therefore, the transverse force and normal force increase with the depth as presented in Fig. 12. Compared with pure sliding motion, the transverse forces of rolling motion are smaller, but the normal forces are larger. As mentioned before, the rolling movement pushes the work piece atoms at the leading end of the abrasive downward during polishing [48], thus increasing the normal force but reducing the transverse force accordingly.

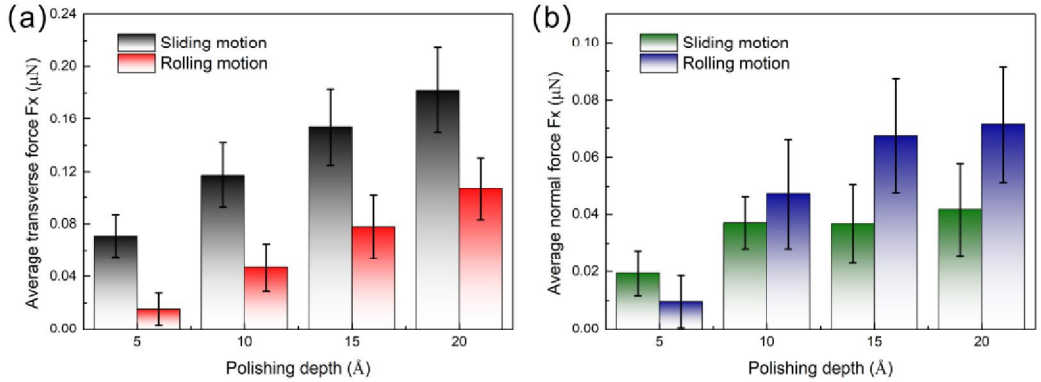

Fig. 12. The curves of (a) the average transverse force and (b) the average normal force (V = 100 m s^{-1}, T = 1 eV).

For a more detailed analysis of the removal and polishing mechanisms during abrasive movement, a schematic diagram of the nano-polishing process is provided in Fig. 13. A critical point A is labeled in the diagram, which lies at a critical or stagnation angle θ with respect to the surface normal, measured in polishing direction. This angle θ is related to the critical atomic layer for forming a chip, and thus corresponds to the minimum uncut chip thickness h_{min}. Here we show that during nano-polishing of Invar, the wear mechanism is highly dependent on the position of point A. Different material removal mechanisms below and above point A (adhering, plowing and cutting, respectively) are considered in the formulation of the forces. When $h < h_{min}$, the sliding removal mechanism is mainly plowing. Given the infinitesimal forces on the abrasive

edge during the plowing process, the adhesion friction coefficient is considered. With a simple force model for material plowing below the stagnation point as shown in Fig. 13(c), there are two forces, namely the horizontal component dF_{px} and the vertical component dF_{pz}, that can be expressed via the following equations [67, 68]:

$$\frac{dF_{px}}{dF_{pz}} = \frac{P_p dA(\sin\theta + \mu_a \cos\theta)}{P_p dA(\cos\theta - \mu_a \sin\theta)} = \tan(\theta + \beta_p), \quad (1)$$

where P_p is the normal stress on the rounded tool edge, $dA = wRd\theta$ is the normal contact area, w is the processing width of the abrasive, R is the abrasive radius, $\mu_a = tan\beta_p$ is the adhesion friction coefficient, and β_p is the friction angle between the abrasive and the uncut work piece.

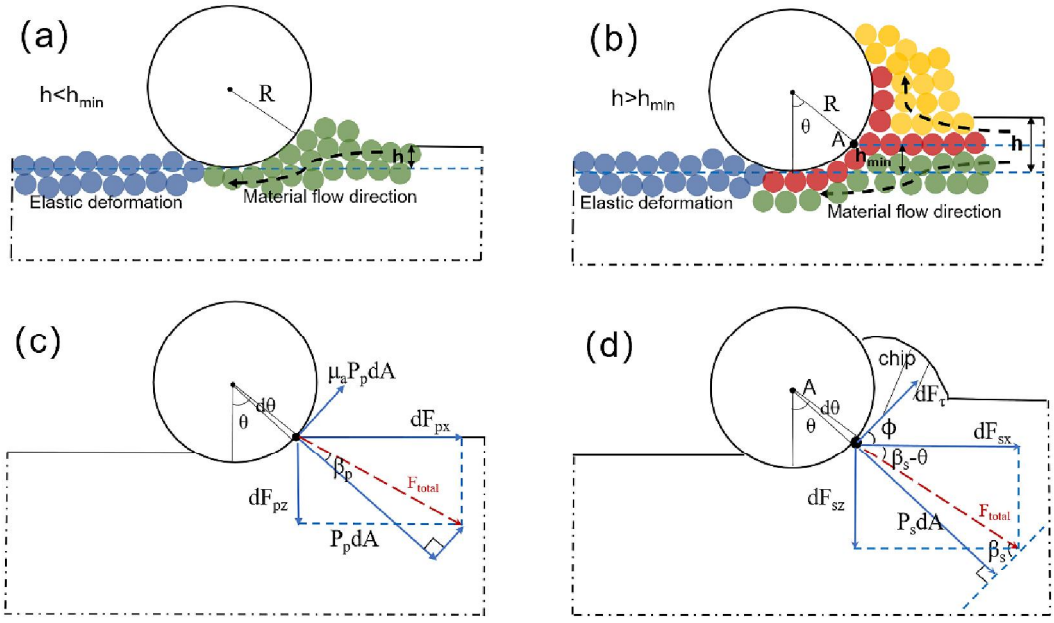

Fig. 13. Schematic diagram for material removal mechanism (a) and (b): $h<h_{min}$, (c) and (d): $h>h_{min}$.

When $h>h_{min}$, the larger shear stress leads to chip formation as shown in Fig. 13(d). Assuming the conventional shear cutting force model, the horizontal component dF_{sx} and the vertical component dF_{sz} can be determined from the following equations [68, 69]:

$$dF_{sx} = \frac{\tau w R \sin\theta \cos(\beta_s - \theta)}{\sin\phi \cos(\phi + \beta_s - \theta)} d\theta \tag{2}$$

$$dF_{sz} = \frac{\tau w R \sin\theta \sin(\beta_s - \theta)}{\sin\phi \cos(\phi + \beta_s - \theta)} d\theta \tag{3}$$

$$\frac{dF_{sx}}{dF_{sz}} = \cot(\beta_s - \theta) \ , \tag{4}$$

where τ is the shear strength, β_s is the friction angle between the tool and a continuous chip, and ϕ is the shear angle.

Complying the force equilibrium, an equation of stagnation angle θ is derived, with the shear angle ϕ being assumed to be almost equal to the stagnation angle θ in sliding motion [68]:

$$\frac{dF_{sx}}{d\tau r d\theta \cos\theta} = \frac{dF_{sz}}{d\tau r d\theta sin\theta} \tag{5}$$

Combining Eq. (4) into Eq. (5), the following equation is obtained:

$$\cot(\beta_s - \theta) = \cot\theta \tag{6}$$

$$\theta = \frac{\beta_s}{2} \tag{7}$$

Therefore, the minimum cutting thickness in sliding motion is determined by:

$$h_{\min} = R(1 - \cos(\theta)) = R(1 - \cos(\frac{\beta_s}{2})) \tag{8}$$

To allow better calculate the θ, the model of abrasive–work-piece contact is employed as shown in Fig. 14. In this study, based on the geometry in Fig. 13(d), we obtain:

$$\beta_s - \theta = \cot^{-1}\frac{F_{sx}}{F_{sz}} \tag{9}$$

Substituting Eq. (7) into Eq. (9), θ is described as:

$$\theta = \cot^{-1}\frac{F_{sx}}{F_{sz}} = \cot^{-1}\mu_{total} \tag{10}$$

Therefore, by simply recasting Eq. (8), the minimum cutting thickness can be written as a function of friction coefficient:

$$h_{\min} = R(1 - \cos(\cot^{-1}\mu_{total})) \tag{11}$$

The apparent friction coefficient can be approximately obtained as the sum of the adhesion and plowing components [70]. When the work piece is in the elastic deformation stage, the friction coefficient can be obtained via Hertzian contact theory [71]:

$$\mu_{el} = \frac{\tau\pi}{F_{sz}^{\frac{1}{3}}} \left(\frac{3R}{4E^*}\right)^{\frac{2}{3}}, \tag{12}$$

where $E^* = [(1-v_i^2)/E_i + (1-v_s^2)/E_s]^{-1}$ is the reduced elastic modulus and E_i, v_i, E_s, v_s represent the elastic moduli and Poisson's ratios of diamond abrasive and Invar, respectively.

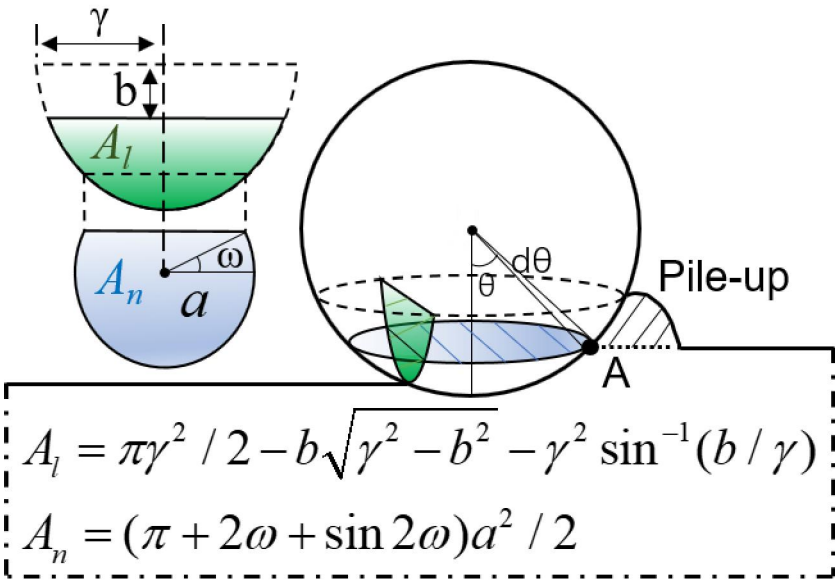

Fig. 14. Schematic illustration of abrasive–work-piece contact configuration at $h = h_{min}$.

When h is close to or exceeds h_{min}, the work piece is in the plastic deformation stage. In order to pursue a more accurate description of the plowing friction coefficient μ_{pl}, Lafaye et al. [72] incorporated the effect of elastic recovery into the calculation of the effective projected areas A_l and A_n based on Goddard and Wilman's model. Their results yield:

$$\mu_{pl} = \frac{A_l}{A_n} = \frac{2}{a^2} \frac{\gamma^2 \cdot \sin^{-1}(a\cos\omega/\gamma) - \sqrt{R^2 - a^2} \cdot a\cos\omega}{\pi + 2\omega + \sin 2\omega}, \quad (13)$$

where $a = \sqrt{2hR - h^2}$ is the contact radius, h is the penetration depth, $\omega = \sin^{-1}\sqrt{2H(R-h)/aE^*}$ is the rear angle accounting for the elastic recovery, H is the hardness of the work piece, and $\gamma = \sqrt{R^2 - a^2\sin^2\omega}$ is considered as a fictive radius of the abrasive.

In fact, during the polishing process, work piece pile-up or a chip is formed in front of the abrasive, increasing the real contact area A_l as shown in Fig. 14. The accumulated atoms ahead would increase plowing friction, which must be considered. When the polishing depth is close to h_{min}, the front pile-up height will reach a stable value with increasing polishing distance due to the side-flow of the protruding material [73]. Based on our simulation results, the accumulation height of pile-up in the plowing regime is approximately 1.5 times the polishing depth. Then Eq. (13) is modified as:

$$\mu_{pl} = \frac{A_l}{A_n} = \frac{2}{a^2} \frac{\pi\gamma^2/2 - b\sqrt{\gamma^2 - b^2} - \gamma^2 \sin^{-1}(b/\gamma)}{\pi + 2\omega + \sin 2\omega}, \quad (14)$$

with $b = \sqrt{\gamma^2 - a^2\cos^2\omega} - 1.5h$ indicating the vertical distance between the pile-up tip and the center of the abrasive.

By adding Eq. (12) and Eq. (14), the total friction coefficient is obtained:

$$\mu_{total} = \mu_{pl} + \mu_{el} = \frac{2}{a^2} \frac{\pi\gamma^2/2 - b\sqrt{\gamma^2 - b^2} - \gamma^2 \sin^{-1}(b/\gamma)}{\pi + 2\omega + \sin 2\omega} + \frac{\tau\pi}{F_{sz}^{\frac{1}{3}}} \left(\frac{3R}{4E^*}\right)^{\frac{2}{3}} \quad (15)$$

For Invar, the elastic modulus, Poisson's ratio, shear strength and hardness obtained by experiments are 123 GPa, 0.27, 348 MPa and 1.46 GPa, respectively. Therefore, according to Eq. (15) and Eq. (10), μ_{total} and θ are calculated to be 1.07 and 43° at a polishing depth of h_{min} (Fig. 14). The obtained minimum uncut chip thickness (5.4 Å), derived based on Eq. (11), is consistent with the results of our simulation (5–

6 Å) in sliding motion. The result for sliding motion confirms the consistency and reasonability of the simulation and the theoretical analysis in this study. On the other hand, due to the complex motion of the abrasive during rolling motion, it is difficult to derive the exact value of the stagnation angle by means of classical mechanical relations. Although the above analysis is building on a basis for sliding motion, we believe that the simulation results can help to predict h_{min} during rotation.

Considering that the minimum uncut chip thickness determines whether a chip is formed or not, it significantly affects the machining efficiency and the surface quality of the work piece, and thus contributing to the understanding of the nano-polishing mechanism in the material removal process. As a final note, the above findings imply that the minimum uncut chip thickness model can be determined from the stagnation angle, which is related to the friction angle and the abrasive radius. Therefore, the minimum uncut chip thickness can be identified approximately from the experimental cutting tests by identifying the friction angle. Furthermore, the model identifies the main parameters that affect the minimum cutting chip thickness. For a given abrasive radius and a surface crystal orientation, h_{min} will therefore depend on the shear strength, elastic moduli and hardness of the processed materials.

5. Conclusion

In this study we investigated the effects of polishing motion on the surface deformation and removal mechanism of an Invar work piece using MD simulations. The influence of the polishing parameters on polishing quality can be summarized as follows:

(1) In the MD simulations, increasing the polishing speed resulted in a higher MRR and reduced subsurface damage, but generated a rougher groove surface and promoted the formation of amorphous regions. With further speed increase, the

polishing efficiency reached a critical value. Comparative validation results of experiments and simulations showed that the variation of MRR and surface roughness exhibit the same trend with different polishing speeds.

(2) When polishing with rolling abrasives, increasing the rolling torque led to an increase in work piece temperature and a decrease in polishing force and MRR. The polishing quality can be optimized by applying the appropriate rolling torque, which however sacrifices MRR.

(3) Compared to sliding motion, the rolling motion generates higher temperatures, lower MRR and a rougher surface morphology, and an appropriate increase of abrasive torque can reduce the thickness of the SDL. At greater polishing depth, the main removal mechanisms of the pure sliding process are plowing removal and cutting removal. In rolling motion, plowing is only present at greater polishing depth, and the plowing regime signals are not as strong as for pure sliding movement.

(4) An expression for the minimum uncut chip thickness leading to the formation of chips was obtained based on the conventional shear cutting force model and abrasive–work-piece contact model. The plastic-deformation-induced chip formation during the nano-polishing process can be used to better identify the material removal mechanism considering the influence of material properties.

Acknowledgments

The authors would like to thank the Natural Science Foundation of China [52175188]; strengthening the foundations project [2020-JCJQ-ZD-111-00-03]; State Key Laboratory for Mechanical Behavior of Materials [20222412]; the Fundamental Research Funds for the Central Universities [3102019JC001]; and SJE acknowledges financial support from the Austrian COMET-Program (Project K2 InTribology1)

[872176].

References

[1] Guillaume CE. Invar and its applications. Nature 1904;71:134-139.

[2] Sahoo A, Medicherla VRR. Fe-Ni Invar alloys: A review. Mater Today: Proc 2021;43:2242-2244.

[3] Schilfgaarde van M, Abrikosov IA, Johansson B. Origin of the Invar effect in iron–nickel alloys. Nature 1999;400:46-49.

[4] X. Zhan, X. Liu, Y. Wei, J. Chen, J. Chen, H. Liu, Microstructure and property characteristics of thick Invar alloy plate joints using weave bead welding, J Mater Process Tech 2017;244:97-105.

[5] Nagayama T, Yamamoto T, Nakamura T. Thermal expansions and mechanical properties of electrodeposited Fe–Ni alloys in the Invar composition range. Electrochim Acta 2016;205:178-187.

[6] Zhao G, Huang C, He N, Liu H, Zou B. Preparation and cutting performance of reactively hot pressed TiB_2-SiC ceramic tool when machining Invar36 alloy. Int J Adv Manuf Tech. 2016;86:2679-2688.

[7] Kim SH, Choi SG, Choi WK, Yang BY, Lee ES. Pulse electrochemical machining on Invar alloy: Optical microscopic/SEM and non-contact 3D measurement study of surface analyses. Appl Surf Sci 2014;314:822-831.

[8] Zhou Q, Han W, Luo D, Du Y, Xie J, Wang X-Z, et al. Mechanical and tribological properties of Zr–Cu–Ni–Al bulk metallic glasses with dual-phase structure. Wear 2021;474-475:203880.

[9] Wang L, Zhou P, Yan Y, Hou C, Guo D. Micro-scale contact behavior and its effect on the material removal process during chemical mechanical polishing. Tribol Int 2021;156:106831.

[10] Huang S, Li X, Mu D, Cui C, Huang H, Huang H. Polishing performance and mechanism of a water-based nanosuspension using diamond particles and GO nanosheets as additives. Tribol Int 2021;164:107241.

[11] Guo J, Gong J, Shi P, Xiao C, Jiang L, Chen L, et al. Study on the polishing

mechanism of pH-dependent tribochemical removal in CMP of CaF_2 crystal. Tribol Int 2020;150:106370.

[12] Luo D, Zhou Q, Ye W, Ren Y, Greiner C, He Y, et al. Design and Characterization of Self-Lubricating Refractory High Entropy Alloy-Based Multilayered Films. ACS Appl Mater Interfaces 2021;13:55712-55725.

[13] Zhu W-L, Beaucamp A. Compliant grinding and polishing: A review. Int J Mach Tool Manu 2020;158:103634.

[14] Fang F, Lai M, Wang J, Luo X, Yan J, Yan Y. Nanometric cutting: Mechanisms, practices and future perspectives. Int J Mach Tool Manu 2022;178:103905.

[15] Li J, Fang Q, Zhang L, Liu Y. Subsurface damage mechanism of high speed grinding process in single crystal silicon revealed by atomistic simulations. Appl Surf Sci 2015;324:464-474.

[16] Ren J, Hao M, Lv M, Wang S, Zhu B. Molecular dynamics research on ultra-high-speed grinding mechanism of monocrystalline nickel. Appl Surf Sci 2018;455:629-634.

[17] Li P, Guo X, Yuan S, Li M, Kang R, Guo D. Effects of grinding speeds on the subsurface damage of single crystal silicon based on molecular dynamics simulations. Appl Surf Sci 2021;554:149668.

[18] Pei QX, Lu C, Lee HP. Large scale molecular dynamics study of nanometric machining of copper. Comput Mater Sci 2007;41:177-185.

[19] Eder SJ, Grützmacher PG, Spenger T, Heckes H, Rojacz H, Nevosad A, Haas F. Experimentally validated atomistic simulation of the effect of relevant grinding parameters on work piece topography, internal stresses, and microstructure. Friction, 2021;10:608-629.

[20] Guo J, Tan S, Xiao C. Atomistic understanding of scratching-induced material attrition of wurtzite single-crystal AlN using nanoscale diamond abrasive. Tribol Int 2022;169:107483.

[21] Yang YH, Zhao HW, Liu HD, Zhang L. A study of abrasive rotating velocity effect on monocrystalline silicon in ultra-precision mechanical polishing via molecular dynamic simulation. Key Eng Mater 2014;609-610:362-369.

[22] Nguyen V-T, Fang T-H. Molecular dynamics simulation of abrasive characteristics

and interfaces in chemical mechanical polishing. Appl Surf Sci 2020;509:144676.
[23] Zhou P, Zhu N, Xu C, Niu F, Li J, Zhu Y. Mechanical removal of SiC by multi-abrasive particles in fixed abrasive polishing using molecular dynamics simulation. Comput Mater Sci 2021;191:110311.
[24] Wu Z, Zhang L, Yang S, Wu C. Effects of grain size and protrusion height on the surface integrity generation in the nanogrinding of 6H-SiC. Tribol Int 2022;171:107563.
[25] Grützmacher P, Gachot C, Eder SJ. Visualization of microstructural mechanisms in nanocrystalline ferrite during grinding. Mater Design 2020;195:109053.
[26] Chen R, Li S, Wang Z, Lu X. Mechanical model of single abrasive during chemical mechanical polishing: Molecular dynamics simulation. Tribol Int 2019;133:40-46.
[27] Avila KE, Küchemann S, Alhafez AI, Urbassek HM. Nanoscratching of metallic glasses – An atomistic study. Tribol Int 2019;139:1-11.
[28] Zhang C, Dong Z, Yuan S, Guo X, Kang R, Guo D. Study on subsurface damage mechanism of gallium nitride in nano-grinding. Mater Sci Semicon Proc 2021;128:105760.
[29] Li J, Fang Q, Liu Y, Zhang L. A molecular dynamics investigation into the mechanisms of subsurface damage and material removal of monocrystalline copper subjected to nanoscale high speed grinding. Appl Surf Sci 2014;303:331-343.
[30] Meng B, Yuan D, Xu S. Study on strain rate and heat effect on the removal mechanism of SiC during nano-scratching process by molecular dynamics simulation. Int J Mech Sci 2019;151:724-732.
[31] Yang Y, Zhao H, Zhang L, Shao M, Liu H, Huang H. Molecular dynamics simulation of self-rotation effects on ultra-precision polishing of single-crystal copper. AIP Adv 2013;3:102106.
[32] Plimpton S. Fast parallel algorithms for short-range molecular dynamics. J Comput Phys 1995;117:1-19.
[33] Stukowski A. Visualization and analysis of atomistic simulation data with OVITO–the Open Visualization Tool. Model Simul Mater Sc 2009;18:015012.
[34] Stukowski A, Albe K. Extracting dislocations and non-dislocation crystal defects from atomistic simulation data. Model Simul Mater Sc 2010;18:085001.

[35] Stukowski A, Bulatov VV, Arsenlis A. Automated identification and indexing of dislocations in crystal interfaces. Model Simul Mater Sc 2012;20:085007.

[36] Tsuzuki H, Branicio PS, Rino JP. Structural characterization of deformed crystals by analysis of common atomic neighborhood. Comput Phys Commun 2007;177:518-523.

[37] Wu C, Lee B-J, Su X. Modified embedded-atom interatomic potential for Fe-Ni, Cr-Ni and Fe-Cr-Ni systems. Calphad 2017;57:98-106.

[38] Liu J, Zhen Q, Zhao CJ, Lu WQ. Corrosion Study of iron in liquid lead-bismuth eutectic in accelerator driven system by molecular dynamics method. J Eng Thermophys 2017;38:557-561.

[39] Gao Y, Brodyanski A, Kopnarski M, Urbassek HM. Nanoscratching of iron: A molecular dynamics study of the influence of surface orientation and scratching direction. Comput Mater Sci 2015;103:77-89.

[40] Si L, Guo D, Luo J, Lu X. Monoatomic layer removal mechanism in chemical mechanical polishing process: A molecular dynamics study. J Appl Phys 2010;107:064310.

[41] Zhao D, Lu X. Chemical mechanical polishing: Theory and experiment. Friction 2013;1:306-326.

[42] Dai H, Zhang F, Chen J. A study of ultraprecision mechanical polishing of single-crystal silicon with laser nano-structured diamond abrasive by molecular dynamics simulation. Int J Mech Sci 2019;157-158:254-266.

[43] Xie W, Fang F. Mechanism of atomic and close-to-atomic scale cutting of monocrystalline copper. Appl Surf Sci 2020;503:144239

[44] Zhou Q, Luo D, Hua D, Ye W, Li S, Zou Q, et al. Design and characterization of metallic glass/graphene multilayer with excellent nanowear properties. Friction 2022;1-12.

[45] Jia Q, He W, Hua D, Zhou Q, Du Y, Ren Y, et al. Effects of structure relaxation and surface oxidation on nanoscopic wear behaviors of metallic glass. Acta Mater 2022;232:117934.

[46] Hua D, Zhou Q, Wang W, Li S, Liu X, Wang H. Atomic mechanism on the

mechanical and tribological performance of amorphous/graphene nanolaminates. Tribol Int 165 (2022) 107318.

[47] Fang T-H, Weng C-I, Chang J-G. Molecular dynamics simulation of nano-lithography process using atomic force microscopy. Surf Sci 2002;501:138-147.

[48] Nguyen V-T, Fang T-H. Material removal and wear mechanism in abrasive polishing of SiO_2/SiC using molecular dynamics. Ceram Int 2020;46:21578-21595.

[49] Shi Z, Li B, Sun Z. Study on microstructure evolution of grinding surface of bcc Fe-Ni maraging steel based on molecular dynamics. Appl Surf Sci 2022;573:151493.

[50] Zhang C, Dong Z, Zhang S, Guo X, Yuan S, Jin Z, et al. The deformation mechanism of gallium-faces and nitrogen-faces gallium nitride during nanogrinding, Int J Mech Sci 2022;214:106888.

[51] Wang W, Hua D, Luo D, Zhou Q, Li S, Shi J, et al. Molecular dynamics simulation of deformation mechanism of CoCrNi medium entropy alloy during nanoscratching. Comput Mater Sci 2022;203:111085.

[52] Si L, Guo D, Luo J, Lu X, Xie G. Abrasive rolling effects on material removal and surface finish in chemical mechanical polishing analyzed by molecular dynamics simulation. J Appl Phys 2011;109:084335.

[53] Ahmadi G, Xia X. A model for mechanical wear and abrasive particle adhesion during the chemical mechanical polishing process. J Electrochem Soc 2001;148:G99.

[54] Nguyen V-T, Fang T-H. Abrasive mechanisms and interfacial mechanics of amorphous silicon carbide thin films in chemical-mechanical planarization. J Alloy Compd 2020;845:156100.

[55] Zhang L, Tanaka H. Atomic scale deformation in silicon monocrystals induced by two-body and three-body contact sliding. Tribol Int 1998;31:425-433.

[56] Gao Y, Ruestes CJ, Urbassek HM. Nanoindentation and nanoscratching of iron: Atomistic simulation of dislocation generation and reactions. Comput Mater Sci 2014;90:232-240.

[57] Hua D, Xia Q, Wang W, Zhou Q, Li S, Qian D, et al. Atomistic insights into the deformation mechanism of a CoCrNi medium entropy alloy under nanoindentation. Int J Plasticity 2021;142:102997.

[58] Shi J, Chen J, Wei X, Fang L, Sun K, Sun J, et al. Influence of normal load on the three-body abrasion behaviour of monocrystalline silicon with ellipsoidal particle. RSC Adv 2017;7:30929.

[59] Fang L, Sun K, Shi J, Zhu X, Zhang Y, Chen J, et al. Movement patterns of ellipsoidal particles with different axial ratios in three-body abrasion of monocrystalline copper: a large scale molecular dynamics study. RSC Adv 2017;7:26790-26800.

[60] Zhang J, Li W, Qin R, Chen P, Liu Y, Liu X, et al. An atomic insight into the stoichiometry effect on the tribological behaviors of CrCoNi medium-entropy alloy. Appl Surf Sci 2022;593:153391.

[61] Zhu J, Xiong C, Ma L, Zhou Q, Huang Y, Zhou B, et al. Coupled effect of scratching direction and speed on nano-scratching behavior of single crystalline copper. Tribol Int 2020;150:106385.

[62] S.J. Eder, P.G. Grützmacher, M. Rodríguez Ripoll, C. Gachot, D. Dini. Does speed kill or make friction better?—Designing materials for high velocity sliding. Appl Mater Today 2022;29:101588.

[63] Goel S, Luo X, Agrawal A, Reuben RL. Diamond machining of silicon: A review of advances in molecular dynamics simulation. Int J Mach Tool Manu 2015;88:131-164.

[64] Oliveira de FB, Rodrigues AR, Coelho RT, Souza de AF. Size effect and minimum chip thickness in micromilling. Int J Mach Tool Manu 2015;89:39-54.

[65] Xie W, Fang F. Mechanism of atomic and close-to-atomic scale cutting of monocrystalline copper. Appl Surf Sci 2020;503:144239.

[66] Hua D, Wang W, Luo D, Zhou Q, Li S, Shi J, et al. Molecular dynamics simulation of the tribological performance of amorphous/amorphous nano-laminates. J Mater Sci Tech 2022;105:226-236.

[67] Yuan ZJ, Zhou M, Dong S. Effect of diamond tool sharpness on minimum cutting thickness and cutting surface integrity in ultraprecision machining. J Mater Process Tech 1996;62:327-330.

[68] Son SM, Lim HS, Ahn JH. Effects of the friction coefficient on the minimum cutting thickness in micro cutting. Int J Mach Tool Manu 2005;45:529-535.

[69] Altintas Y. Manufacturing Automation: Metal Cutting Mechanics. Machine Tool Vibrations and CNC Design. Cambridge: Cambridge University Press;2000.

[70] Ye YX, Liu CZ, Wang H, Nieh TG. Friction and wear behavior of a single-phase equiatomic TiZrHfNb high-entropy alloy studied using a nanoscratch technique. Acta Mater 2018;147:78-89.

[71] Johnson KL. Contact Mechanics. Cambridge: Cambridge University Press;1987.

[72] Lafaye S, Gauthier C, Schirrer R. The ploughing friction: analytical model with elastic recovery for a conical tip with a blunted spherical extremity. Tribol Lett 2006;21(2):95-99.

[73] Yang X, Qiu Z, Wang Y. Investigation of material flow behaviour and chip formation mechanism during grinding of glass-ceramics by nanoscratch. Ceram Int 2019;45:15954-15963.